The Astrophysical Journal, 993:206 (13pp), 2025 November 10 https://doi.org/10.3847/1538-4357/ae0ca8

Gravitational Wave Decoupling in Retrograde Circumbinary Disks

David O'Neill[1], Christopher Tiede[1], Daniel J. D'Orazio[1,2,3], Zoltán Haiman[4,5,6], and Andrew MacFadyen[7]
[1] Niels Bohr International Academy, Niels Bohr Institute, Blegdamsvej 17, DK-2100 Copenhagen ∅, Denmark; david.oneill@nbi.ku.dk
[2] Space Telescope Science Institute, 3700 San Martin Drive, Baltimore, MD 21, USA
[3] Department of Physics and Astronomy, Johns Hopkins University, 3400 North Charles Street, Baltimore, MD 21218, USA
[4] Department of Astronomy, Columbia University, 550 West 120th Street, New York, NY 10027, USA
[5] Department of Physics, Columbia University, 550 West 120th Street, New York, NY 10027, USA
[6] Institute of Science and Technology Austria (ISTA), Am Campus 1, Klosterneuburg 3400, Austria
[7] Center for Cosmology and Particle Physics, Physics Department, New York University, New York, NY 10003, USA
Received 2025 January 20; revised 2025 September 22; accepted 2025 September 24; published 2025 November 5

Abstract

We present a study of the late-time interaction between supermassive black hole binaries and retrograde circumbinary disks during the period of gravitational wave-driven inspiral. While mergers in prograde disks have received extensive study, retrograde disks offer distinct dynamics that could promote mergers and produce unique observational signatures. Through 2D numerical hydrodynamical simulations, we explore the process of binary-disk decoupling, where the binary's orbital decay rate is faster than the disk's viscous response rate. We find the point of decoupling to be comparable in prograde and retrograde disks, suggesting that any associated electromagnetic (EM) signatures will be produced at comparable times preceding the merger. However, we find smaller central cavities for retrograde disks, likely leading to higher-frequency EM emissions and shorter postmerger rebrightening timescales compared to their prograde counterparts. Retrograde disks form intrabinary bridges, which are prone to instabilities when the viscosity is low. These instabilities manifest as quasiperiodic flares in the accretion rate, which may produce distinctive EM signatures for retrograde disks.

Unified Astronomy Thesaurus concepts: Gravitational waves (678); Accretion (14); Supermassive black holes (1663); Hydrodynamical simulations (767)

1. Introduction

The gravitational waves (GWs) produced by compact supermassive black hole binaries (SMBHBs) propagate through the Universe, encoded with information of the binary's final moments before merger. The advent of next-generation space-based GW detectors (e.g., the Laser Interferometer Space Antenna (LISA), P. Amaro-Seoane et al. 2023; the Taiji program, W.-H. Ruan et al. 2020; and TianQin Y. Gong et al. 2021) will enable such observations. Accompanied by theoretical modeling, these detections may reveal the nature of their astrophysical environments (P. Amaro-Seoane et al. 2023), fundamental physics in the strong gravity regime (S. Afroz & S. Mukherjee 2024; L. Speri et al. 2024), and the cosmological history of massive mergers (P. Auclair et al. 2023).

GWs alone are inefficient at producing compact SMBHBs. Instead, the external environment is required to reduce the binary separation from the galactic scale ∼kiloparsec to the subparsec gravitational wave inspiral scale (e.g., M. C. Begelman et al. 1980; F. M. Khan et al. 2012; L. Z. Kelley et al. 2017). Following the merger of two massive galaxies, the two remnant cores will sink to the center of the newly formed galaxy via dynamical friction (S. Chandrasekhar 1943; V. Springel et al. 2001; T. DiMatteo et al. 2023), where they will encounter each other and become bound. Stars with orbits intersecting this binary (so-called "loss-cone orbits") can experience a gravitational slingshot, thereby extracting orbital energy from the binary, further reducing its separation (P. Berczik et al. 2006; I. Berentzen et al. 2009). This process will slowly tighten the SMBHB until around $\lesssim$0.1 pc (P. J. Armitage & P. Natarajan 2002) from which point many of these binaries are expected to interact with ambient gas in the galactic nucleus and form a circumbinary accretion disk (J. E. Barnes & L. E. Hernquist 1991; P. Artymowicz & S. H. Lubow 1996; A. I. MacFadyen & M. Milosavljević 2008; T. L. Tanaka & Z. Haiman 2013; L. Mayer 2013). This disk will exert a force on the binary, changing its orbital elements (A. Gould & H.-W. Rix 2000; P. J. Armitage & P. Natarajan 2002; M. S. L. Moody et al. 2019; D. J. D'Orazio & P. C. Duffell 2021; J. Zrake et al. 2021) until gravitational waves become sufficient to drive the binary to merge. These accretion disks are of particular interest because they can source bright multiwavelength EM radiation (K. Gültekin & J. M. Miller 2012; B. Kocsis et al. 2012; J. R. Westernacher-Schneider et al. 2022; D. J. D'Orazio & M. Charisi 2023) with the possibility of remaining bright all the way until merger (B. D. Farris et al. 2015; L. M. Krauth et al. 2023; A. Franchini et al. 2024). For this reason, an observable EM counterpart may accompany an SMBHB merger (J. D. Schnittman & J. H. Krolik 2008; D. B. Bowen et al. 2018; Y. Tang et al. 2018; V. Paschalidis et al. 2021; T. Bogdanović et al. 2022; J.-M. Wang et al. 2022).

An EM signal coincident with a gravitational wave measurement would greatly enhance the significance of the detection (D. E. Holz & S. A. Hughes 2005; N. Tamanini et al. 2016; A. Mangiagli et al. 2022). Complementary to gravitational waves, EM signals would provide much better sky localization, possibly enabling a unique host galaxy to be identified with each event—allowing independent measurements of the merger mass and redshift via their spectra and broad-line regions (e.g., S. Casura et al. 2024). Time-domain surveys of the host galaxies may capture the expected inspiral

signatures, such as an abrupt disappearance of X-rays (as seen in L. M. Krauth et al. 2023), followed by their gradual rebrightening or a brightening in the UV (M. Clyburn & J. Zrake 2024; A. Franchini et al. 2024). Moreover, EM signatures alone could enable indirect detections of SMBHB mergers when gravitational wave detectors are offline or when systems are outside of the detectors' sensitivity range. To quantify the signatures produced, we study circumbinary disks hosting a gravitational wave inspiral.

In a steady-state, the angular momentum of an accretion disk can be either aligned (prograde) or misaligned (retrograde) with the angular momentum vector of the binary. Prograde disks have received extensive attention (e.g., A. I. MacFadyen & M. Milosavljević 2008; J. Cuadra et al. 2009; D. J. D'Orazio et al. 2013, along with all previously referenced circumbinary disk studies), whereas retrograde ones have much less so. A circumbinary accretion disk with random initial inclination θ will counteralign (retrograde) with the binary if $\cos\theta < -J_d/2J_b$ (C. J. Nixon et al. 2011; C. J. Nixon 2012), where $\boldsymbol{J}_d$ and $\boldsymbol{J}_b$ are the disk and binary angular momenta, respectively. Therefore, depending on the nature of the accretion episodes, the retrograde configuration is not only stable, but almost as likely to form as the prograde one when $J_d \ll 2J_b$ (A. R. King & J. E. Pringle 2006; M. C. Miller & J. H. Krolik 2013; J. Bankert et al. 2015). We argue that retrograde disks may be a promising environmental source of SMBHB mergers for a number of reasons:

1. Irrespective of orbital parameters, retrograde disks always facilitate orbital inspiral. In contrast, prograde disks have been observed to produce orbital outspirals under specific disk conditions and binary orbital parameters (D. J. Muñoz et al. 2019; D. J. D'Orazio & P. C. Duffell 2021; M. Siwek et al. 2023).
2. The torque experienced by a binary in a retrograde disk is stronger than in a prograde counterpart (C. Tiede & D. J. D'Orazio 2023, and references therein), facilitating a faster orbital decay (C. J. Nixon et al. 2011; J. D. Schnittman & J. H. Krolik 2015).
3. Unlike prograde disks, eccentricity is always driven for equal-mass binaries[8] in retrograde disks (C. J. Nixon et al. 2011; C. Tiede & D. J. D'Orazio 2023). Larger eccentricities will lead to an earlier onset of the gravitational wave-dominated regime, thereby promoting SMBHB mergers.
4. Large initial eccentricities may not completely circularize before entering detector sensitivity, leaving direct observable consequences (M. Garg et al. 2024b; S. DeLaurentiis et al. 2025).

In this paper, we focus on the process of binary-disk decoupling– defined as the point at which the binary's orbital decay due to gravitational radiation outpaces the disk's ability to viscously react. After decoupling, the binary quickly contracts toward merger, leaving the circumbinary disk behind. Depending on the viscosity of the disk, decoupling can occur at different binary semimajor axes (P. J. Armitage & P. Natarajan 2002) and, therefore, at different times preceding the merger. For a range of different binary masses ($10^4 \rightarrow 10^7 M_\odot$) and typical values for viscosity, A. J. Dittmann et al. (2023) found that high-viscosity prograde disks likely decouple within the LISA band (see their Figure 5), enabling coincident EM and gravitational wave detections of the event. However, despite retrograde disks potentially accounting for a significant portion of SMBHB mergers, decoupling in retrograde disks has remained unexplored. To address this, we perform numerical simulations of the late-time interaction between an equal-mass binary inspiralling within a retrograde circumbinary disk.

We present our analytical and numerical methods in Section 2, followed by our results on disk morphology, accretion rates, torque rates, and binary-disk decoupling in Section 3. In Section 4 we present a discussion of our results, and finally, our conclusions in Section 5.

2. Methods

2.1. Orbital Dynamics

We begin by describing the orbital dynamics of a gravitational wave inspiral. While retrograde disks promote eccentricity growth, we assume that the binary is initially circular ($e = 0$) as a first step to simplify the key dynamics involved in the system. In addition, we assume the binary to be of equal-mass components (with total mass M) and coplanar with the disk ($\iota = 0$). Under these assumptions, the orbital phase ϕ and separation a uniquely determine the binary dynamics. Correspondingly, we adopt the initial semimajor axis a_0 as unit length, along with the initial angular frequency $\Omega_0 = \sqrt{GM/a_0^3}$ as inverse unit time. Following P. C. Peters (1964), we assume that the orbital energy changes over a timescale much longer than the orbital period, permitting an approximation to the quadrupolar formula (A. Einstein 1916) as a series of closed Keplerian orbits. In doing so, the semimajor axis $a(t)$ and orbital phase $\phi(t)$ become time-dependent quantities,

$$\frac{a(t)}{a_0} = \left(1 - \frac{64}{5}\frac{G^3M^3}{a_0^4c^5}t\right)^{\frac{1}{4}} \tag{1}$$

$$\phi(t) = \int_0^t dt' \sqrt{\frac{GM}{a(t')^3}}. \tag{2}$$

Here c is the speed of light, which, when expressed in the unit system above $c = \tilde{c}\, a_0\Omega_0$,

$$\tilde{c} = \sqrt{\frac{c^2 a_0}{GM}} = \sqrt{\frac{a_0}{r_G}}, \tag{3}$$

where r_G is the gravitational radius. The numerical value of $\tilde{c}$ determines the timescale for orbital inspiral. We adopt a fiducial value of $a_0 = 100 r_G$ corresponding to a merger timescale of $t_m \approx 1244 \times 2\pi/\Omega_0$ (approximately 1990 binary orbits). Finally, we neglect relativistic corrections to fluid motion near the black holes and treat the binary components as Plummer potentials,

$$\Phi_b(\boldsymbol{x}) = -\frac{GM}{2\sqrt{|\boldsymbol{x} - \boldsymbol{x}_1|^2 + r_{\rm soft}^2}} - \frac{GM}{2\sqrt{|\boldsymbol{x} - \boldsymbol{x}_2|^2 + r_{\rm soft}^2}}, \tag{4}$$

where $\boldsymbol{x}_1, \boldsymbol{x}_2$ are the current positions of the binary components and $r_{\rm soft}$ is the gravitational softening length.

[8] For a mass ratio of $q = 0.1$, P. Amaro-Seoane et al. (2016) found that initially circular binaries oscillate around eccentricities $e < 0.1$, while initially eccentric binaries become more eccentric.

2.2. Disk Dynamics

We model the disk in 2D as a viscous fluid in the presence of the time-changing gravitational potential of the binary (Φ_b). Hence we solve the vertically integrated mass conservation and Navier–Stokes equations for disk surface density Σ and midplane fluid velocity v^i,

$$\partial_t \Sigma + \partial_i(\Sigma v^i) = S_\Sigma \tag{5}$$

$$\partial_t(\Sigma v^j) + \partial_i(\Sigma v^i v^j + P\delta^{ij} - \tau^{ij}) = S^j - \partial^j \Phi_{\rm b}, \tag{6}$$

where P is the 2D pressure, δ^{ij} is the Kronecker delta, and S_Σ, S^j are the mass and momentum sinks. The viscous stress tensor

$$\tau^{ij} = \nu\Sigma\left(\partial^i v^j + \partial^j v^i - \frac{2}{3}\delta^{ij}\partial_k v^k\right), \tag{7}$$

describes the transport of momentum Σv^i across surfaces of constant j, with ν the kinematic viscosity of the fluid. We assume a locally isothermal equation of state by prescribing the sound speed $c_{\rm s}$ as

$$c_{\rm s}^2 = -\frac{\Phi_b}{\mathcal{M}^2}, \tag{8}$$

for which the vertically integrated pressure is given by $P = \Sigma c_{\rm s}^2$. A locally isothermal equation of state requires that the viscous heating and radial advection timescales are much longer than the radiative cooling timescale. Here, $\mathcal{M} = r/H$ is the constant Mach number in the disk, where H is the vertical scale height of the disk, which we assume to be in vertical hydrostatic equilibrium. In a steady state, this Mach number is approximately equal to the ratio of the gas velocity to the sound speed $\mathcal{M} \sim r\Omega/c_{\rm s}$ at a given point. We adopt a fiducial value of $\mathcal{M} = 10$ for all simulations.

2.3. Decoupling

In this subsection, we introduce an idealized accretion disk whose purpose is to provide an analytical estimate for binary-disk decoupling. We assume that the disk is Keplerian, with net zero angular momentum current and a globally uniform surface density. We parameterize viscous angular momentum transport through the disk with the coefficient of kinematic viscosity, ν, for which the viscous transport of angular momentum leads to an inward flow of mass with radial velocity

$$v_{\rm r} = -\frac{3\nu}{2r}. \tag{9}$$

Equation (9) sets a "viscous rate" determining the timescale required for gas to rearrange its angular momentum and reorient itself across the disk. The moment at which the rate of change of binary semimajor axis (the derivative of Equation (1)) is equal to the radial velocity due to viscosity (Equation (9)) is the final time that the disk is viscously coupled to the gas at some given reference radius $r = \xi a_{\rm b}$. Therefore, the binary and the idealized disk decouple at semimajor axis $a_{\rm dc}$,

$$a_{\rm dc} = \sqrt{\frac{32\xi}{15\nu}\frac{G^3M^3}{c^5}}. \tag{10}$$

This velocity-based argument for decoupling agrees with numerical simulations of inspirals in prograde disks (see Figure 2 of A. J. Dittmann et al. 2023, where the reference radius is taken to be the cavity radius $\xi \sim 2$–3).

2.4. Numerical Methods

All simulations were performed using the publicly available, GPU-accelerated code, `Sailfish` (for further details, see J. Zrake & A. MacFadyen 2024, and P. C. Duffell et al. 2024 for a code comparison). `Sailfish` is a second-order, Newtonian, grid-based hydrodynamics code designed to solve Equations (5) and (6) numerically on a fixed Cartesian grid. Below, we discuss our main numerical methods.

The computational domain is a 2D Cartesian grid of size $20a_0 \times 20a_0$ with resolution $n = 3000 \times 3000$. Centered on this domain is a circular outer-boundary "buffer region" of radius $9a_0$—outside of which, the solution is damped back to that of a steady-state, axisymmetric accretion disk (J. R. Westernacher-Schneider et al. 2022). The softened Plummer potentials Equation (4) represent inner boundaries wherein mass and momentum sinks S_Σ, S^j emulate the accretion of material onto the binary. We use an acceleration-free sink prescription (A. J. Dittmann & G. Ryan 2021) in modeling a physical horizon-like boundary which removes mass and momentum at a rate of $\gamma_{\rm sink} = 50\,\Omega_0$ motivated by matching the sink timescale with the viscous timescale at the sink radius (for further discussion see Section 3.2), with radius equal to the Innermost Stable Circular Orbit (ISCO) $r_{\rm sink} = 0.03a_0$ (and softening length $r_{\rm soft} = 0.03a_0$, unless specified otherwise). The cell spacing is $\delta \approx 0.0067a_0$, meaning that there are ~63 cells covering the area of the sink.

We initialize each simulation with a uniform density profile $\Sigma/\Sigma_0 = 1$ and allow the disk to viscously relax for 1000 binary orbital periods prior to the onset of a gravitational wave inspiral. During this relaxation period, we implement a gentle sink for the first 800 binary orbits with a rate $\gamma_{\rm sink} = 1\,\Omega_0$. We find this gentle-sink period to be necessary for the numerical stability of the solution at the beginning of the simulation. We perform both prograde and retrograde simulations, which are identical other than the initial azimuthal flow of the gas over a range of different kinematic viscosities, $\nu = \tilde{\nu}\ \ a_0^2\Omega_0$ where $\tilde{\nu} \in \{10^{-4}, 3\times10^{-4}, 10^{-3}, 3\times10^{-3}, 10^{-2}\}$.[9]

3. Results

3.1. Disk Morphology

During the inspiral, the disk evolves in response to the binary. We illustrate this evolution through 2D surface density profiles in Figure 1 and the azimuthally averaged density profiles in Figure 2 for a selection of different times and viscosities.

Perhaps the most prominent feature of a circumbinary disk is the central cavity, a low-density region of the disk, excavated by the binary. In the left panels of Figure 1, we approximate the cavity (see Appendix) as an ellipse with semimajor axis $a_{\rm c} \approx a_0$ and eccentricity $e_{\rm c} \approx 0.4$–0.8 centered and oriented with the binary. The cavity semimajor axis $a_{\rm c} \approx a_0$ is significantly smaller than typical prograde values

[9] These constant kinematic viscosities correspond to α-viscosity models (N. I. Shakura & R. A. Sunyaev 1973) of $\alpha \in [10^{-2}, 3\times10^{-2}, 10^{-1}, 3\times10^{-1}, 1]$ when evaluated at the binary semimajor axis.

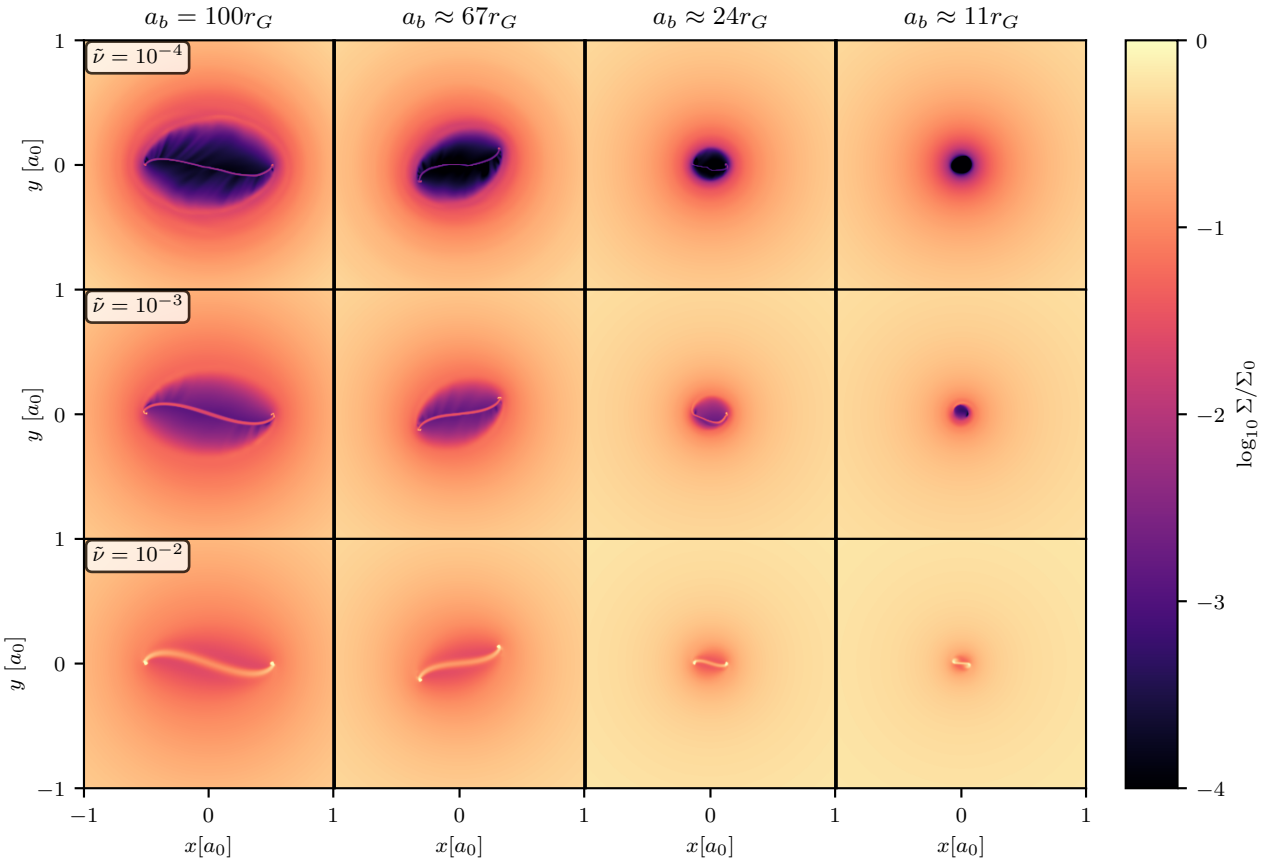

Figure 1. Logarithmic snapshots of the disk surface density Σ/Σ_0 across a range of binary semimajor axes (columns) and viscosities (rows). The left-most panels illustrate the disk structure following the viscous relaxation period of 1000 binary orbits—preceding the onset of a gravitational wave inspiral. As the inspiral progresses, the semimajor axis of the binary decreases (right) and the disk reacts, primarily through a shrinking central cavity. Decoupling happens earlier for less viscous disks (top) while the intrabinary bridge is more stable for larger viscosities (bottom).

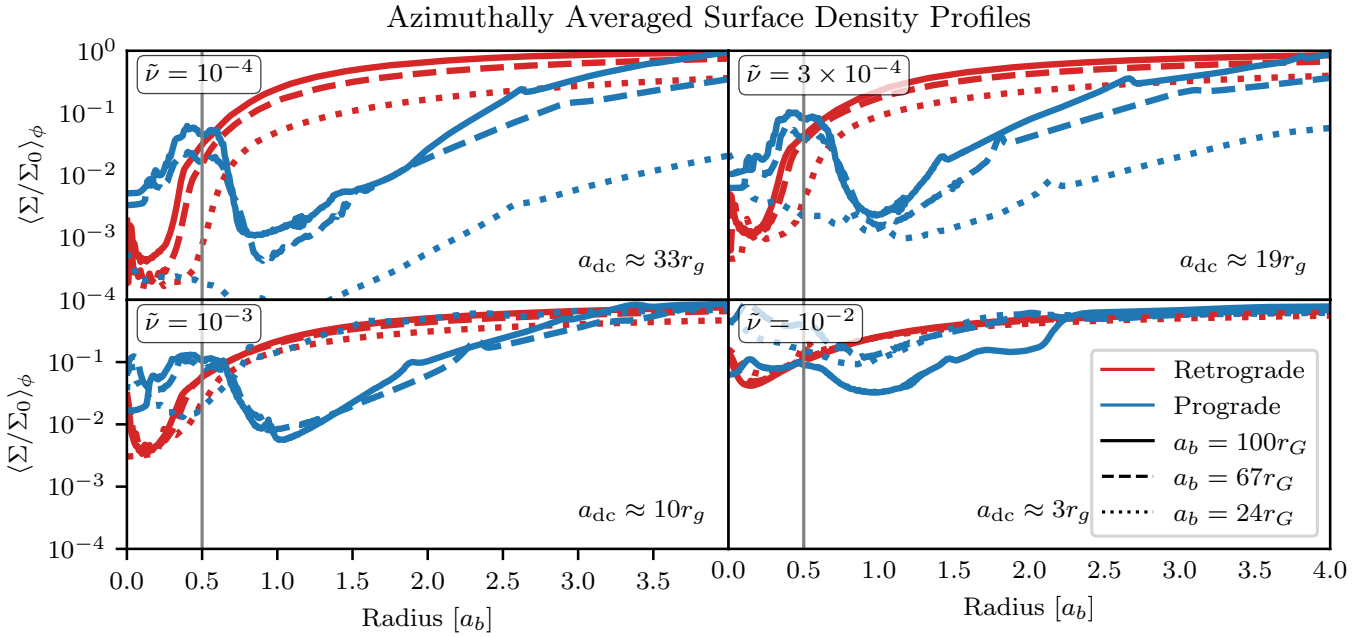

Figure 2. Azimuthally averaged surface densities for retrograde disks (red) and prograde disks (blue) at three different stages during the inspiral (solid, dashed, and dotted). The x-axis units have been scaled to the current orbital separation of the binary (gray vertical lines). On each panel, we print the nominal decoupling semimajor axis $a_{\rm dc}$ (see Equation (10) with $\xi = 0.6$).

between $2a_0$ and $5a_0$ (K. Hirsh et al. 2020), suggesting that a retrograde circumbinary disk can remain stable much closer to the binary than a prograde disk can (e.g., C. Roedig & A. Sesana 2014, for further discussion, see Section 4.1 on the stability of retrograde orbits). The cavity orientation locks with the binary before the inspiral (C. Tiede & D. J. D'Orazio 2023)

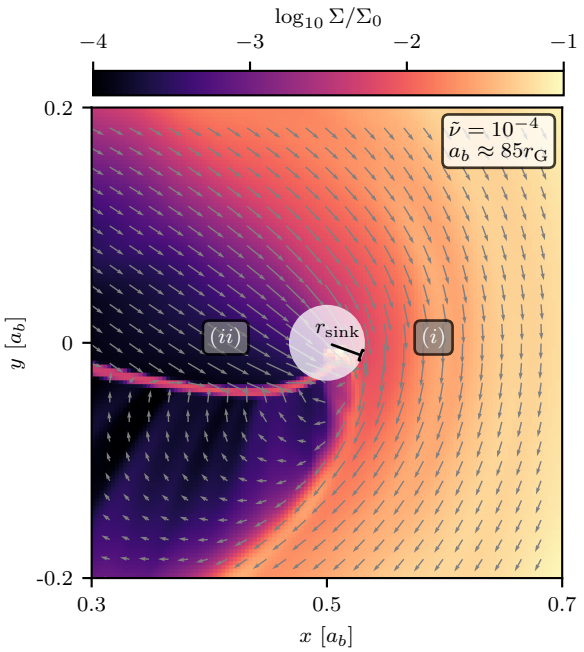

Figure 3. Zoom in on one of the binary components. The arrows represent the direction of fluid velocity in the frame corotating with the binary, and the colormap is the logarithmic surface density. Regions (i) and (ii) experience significant deflections by the binary and collide, forming a shock behind each binary component.

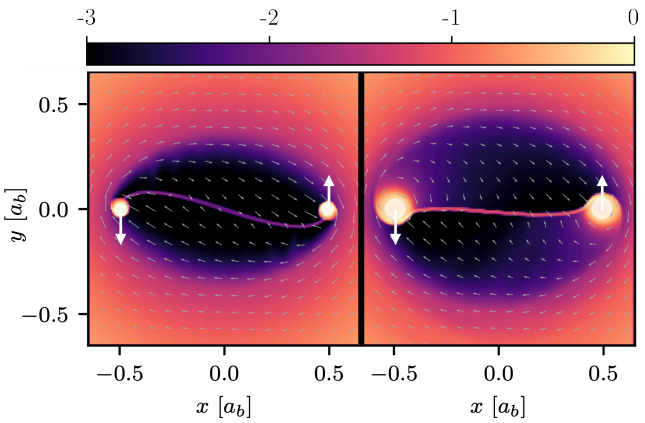

Figure 4. Two stable minidisk configurations for $\gamma_{\rm sink} = 1\,\Omega_0$, corresponding to different values of the softening radius, $r_{\rm soft} = 0.03a_0$ (left) and $r_{\rm soft} = 0.05a_0$ (right) in otherwise identical simulations. These density snapshots are taken at $t = 200[2\pi\Omega_0^{-1}]$ with the large white arrows depicting the direction of motion of the binary.

and during the early stages of the inspiral (left panels of Figure 1), while at later times (as the binary approaches merger), the cavity drops in eccentricity, becoming more axisymmetric meaning that information on the cavity's orientation is lost (right panels of Figure 1). In contrast, lopsided, eccentric cavities ($e \approx 0.05$–0.35 E. Ragusa et al. 2020) persist during inspiral for prograde configurations as seen in Figure 1 of both A. J. Dittmann et al. (2023) and L. M. Krauth et al. (2023).

In Figure 2 we illustrate the azimuthally averaged surface density profiles $\langle\Sigma/\Sigma_0\rangle_\phi$ across a range of viscosities and times. We draw comparisons to reference prograde disks (blue) to better understand the qualitative differences in disk structure throughout the inspiral. Retrograde disks maintain a larger surface density closer to the binary, virtue of a smaller cavity—with the notable exception of the prograde minidisks (the blue bumps near $r = 0.5a_{\rm b}$). As the viscosity increases (lower right panel), the disk becomes increasingly capable of retaining its initial surface density profile throughout the inspiral. Retrograde disks also exhibit smoother surface density profiles than their prograde counterparts.

An intrabinary bridge is present in a selection of panels from Figure 1. As the binary rotates along its orbit, it approaches circumbinary disk material, which is exterior to the binary orbit (region (i) of Figure 3), and cavity material, which is interior to the binary orbit (region (ii) of Figure 3). Particularly close encounters between the gas and the binary result in the deflection of material, although in opposite directions for regions (i) and (ii). As a result, two opposing streams of material collide behind each binary component ($y < 0$ in Figure 3) and a shock is formed. The locations at which these shocks occur constitute the intrabinary bridge with a characteristic "S" shape. Material on this bridge has low angular momentum and can be transported almost radially before being accreted. In Section 4.2 we discuss the stability of the intrabinary bridge for low-viscosity retrograde disks.

3.2. Minidisks

The lack of circumsingle minidisks during retrograde simulations is evident in Figures 1–2. Previous studies have debated their existence, with C. Tiede & D. J. D'Orazio (2023) and C. J. Nixon (2012) finding persistent minidisks, whereas C. Roedig & A. Sesana (2014) did not. During our retrograde simulations, we observe minidisks only during the "gentle-sink" relaxation phase.

For a low sink rate ($\gamma_{\rm sink} = 1\,\Omega_0$), we observe two different stable solutions determined by the softening radius $r_{\rm soft}$, as illustrated in Figure 4. On the one hand, a large softening radius ($r_{\rm soft} = 0.05a_0$, right panel) results in a shallow gravitational potential, allowing bound material to spread over a wider area, resulting in broader minidisks. As these wide minidisks rotate through the cavity, substantial ram pressure generates shocks which cause the intrabinary bridge to attach to the front of the minidisk, rather than to the rear. On the other hand, a small softening radius results in smaller minidisks, which are attached to the rear by the intrabinary bridge (left). We verified that larger sink radii ($r_{\rm sink} = 0.05a_0$) have no effect on the size of the minidisks or the structure of the intrabinary bridge.

The bridge is the funnel through which material is channeled onto the minidisk. Front-attaching bridges (right panel of 4) source retrograde minidisks, whereas rear-attaching bridges (see left panel of Figure 3) source prograde minidisks. Therefore, for a low sink rate ($\gamma_{\rm sink} = 1\,\Omega_0$), the size of the minidisks, their sense of rotation, and the intrabinary bridge connecting them can be in different, stable configurations depending on the softening radius.

We note that prograde circumbinary disks host larger minidisks than retrograde circumbinary disks—with typical radii of $\mathcal{R}_{\rm P} \approx 0.3a_0$ for the former and $\mathcal{R}_{\rm R} \approx 0.1a_0$ for the latter (right panel Figure 4). The origin of this difference may be attributed to the size of the Roche-bound region, defined to be the region within which material is gravitationally bound to an individual component of the binary. For further discussion, see Section 4.1 below.

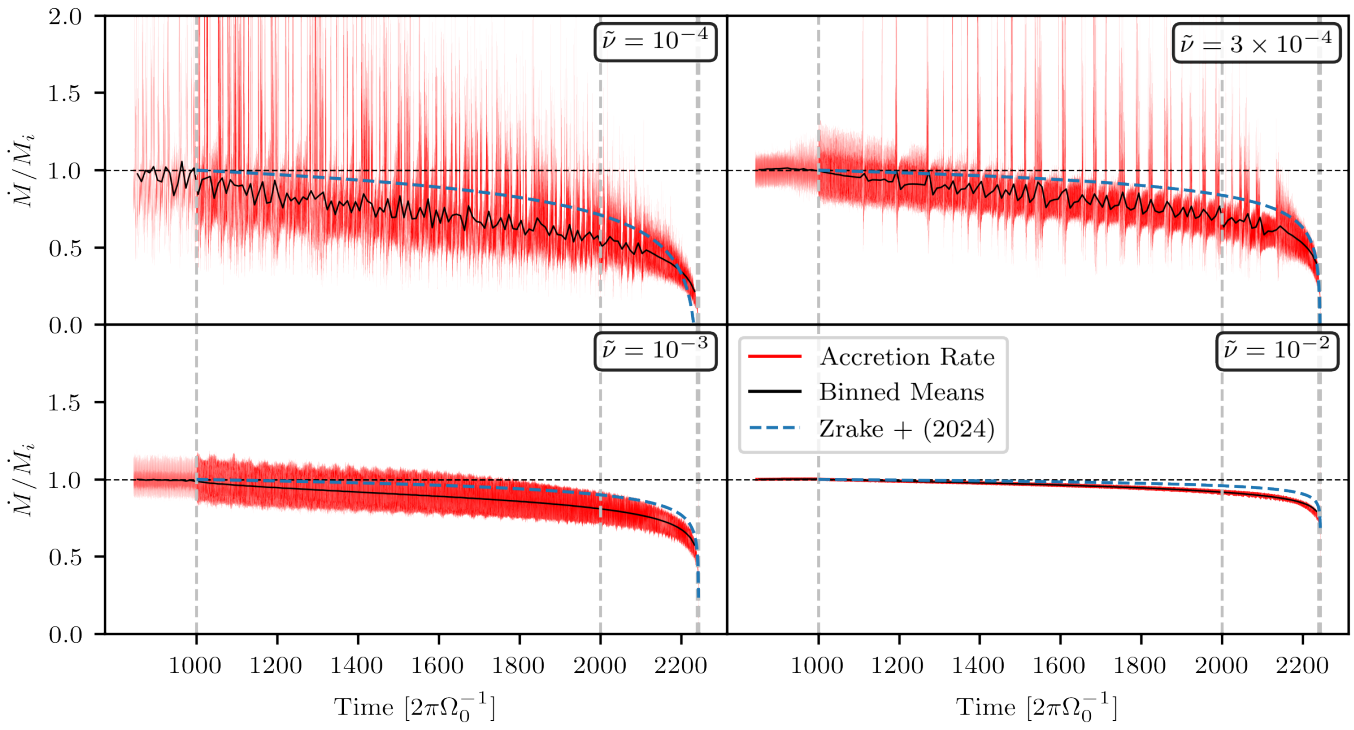

Figure 5. Total accretion rates $\dot{M} = \dot{M}_1 + \dot{M}_2$ of retrograde binaries for the viscosities noted in the top right of each panel. The inspiral is initiated at $t = 1000 \quad [2\pi\Omega_0^{-1}]$ orbits, at which time the time series cadence is also increased. The dashed gray lines correspond to the times at which the density snapshots are taken in Figure 1 (i.e., $a_b = [100r_G, 67r_G, 24r_G, 11r_G]$) in all panels. The accretion rate is normalized to unity in each panel, with $\dot{M}_i > 3\pi\nu\Sigma_0$ (this overshoot is discussed in M. Clyburn & J. Zrake 2024 and attributed to an artifact of the outer boundary). The dashed blue lines represent the "weakening-torque effect" from J. Zrake et al. (2025).

For large initial binary separations ($a_0 \gg 100r_G$), the ISCO is a difficult scale to numerically resolve. As such, the mass and momentum sinks emulate the accretion of material onto the binary. However, for small initial binary separations ($a_0 = 100r_G$), the scale of the ISCO can be numerically resolved, providing physical inner boundary conditions. Therefore, the sink rate must be sufficiently high to ensure that once material crosses the inner boundary, it is swiftly removed from the domain to prevent artificial pile-ups. Irrespective of the softening radius of the disks, when a faster sink is implemented ($\gamma_{\rm sink} = 50\,\Omega_0$), the resulting solution always features a rear-attaching bridge without circumsingle minidisks—as depicted in Figure 3. For completeness, we verified that higher sink rates have no effect on the simulation results of prograde disks.

3.3. Accretion and Torque Time Series

The total accretion rates ($\dot{M}$) and the torques exerted on the disk ($\mathcal{T}$) are computed as runtime diagnostics in `Sailfish`. The total torque exerted on the disk is composed of both a gravitational $\mathcal{T}_g$ and an accretion $\mathcal{T}_a$ component (see Section 4.1 of P. C. Duffell et al. 2024, for further details). We present these time series data for a selection of different viscosities in Figures 5, 6, and 7.

The total accretion rate for low-viscosity disks (top row of Figure 5) exhibits irregular structure with strong variability. We note that during the "gentle-sink" relaxation period, the accretion rates are smoother, which we attribute to the presence of the minidisks[10] which regulate the flow of material around the sink. Once the sink rate is increased and the buffer of the minidisks is lost, interesting behavior manifests through quasiperiodic accretion "flares" (most visible in the upper right panel of Figure 5). Typically, this consists of an initially quiescent period of steady accretion, which gradually rises before culminating in a sharp flare (see also Figure 11). These flares soon subside, facilitating a return to a steady, quiescent accretion after a few binary orbits. We attribute these flares to phases of instability in the intrabinary bridge, which we discuss further in Section 4.2. With increasing viscosity comes more regular accretion behavior, which we attribute to viscosity's role as a damping mechanism.

The binary accretion rates steadily decline following the onset of GW-driven inspiral in all panels of Figure 5. This secular decline can be attributed to (i) a lack of supply due to inadequate viscous transport of material or (ii) the "weakening-torque effect" (J. Zrake et al. 2025), where a time-varying torque $\mathcal{T}$ exerted by the binary alters the disk structure, causing long-term trends in the accretion rate. If one considers the relative radial velocity between the binary and an annulus of gas at radius r, at some r this relative velocity will be too slow to adequately replenish regions interior to r. That is, before the nominal point of decoupling, the binary successively loses viscous contact with each annulus in the disk (from outside in), restricting the viscous inflow of material during inspiral. For example, lower viscosity disks are unable to retain their initial surface density profile during inspiral in Figure 2, limiting the amount of gas available to be accreted, and slowly "starving" the binary—even before the nominal point of decoupling. In contrast, the larger viscosity $\tilde{\nu} = 10^{-2}$ systems (bottom right panel) retain their initial density profiles

[10] These are only present during the gentle-sink period, $\gamma_{\rm sink} = 1\,\Omega_0$.

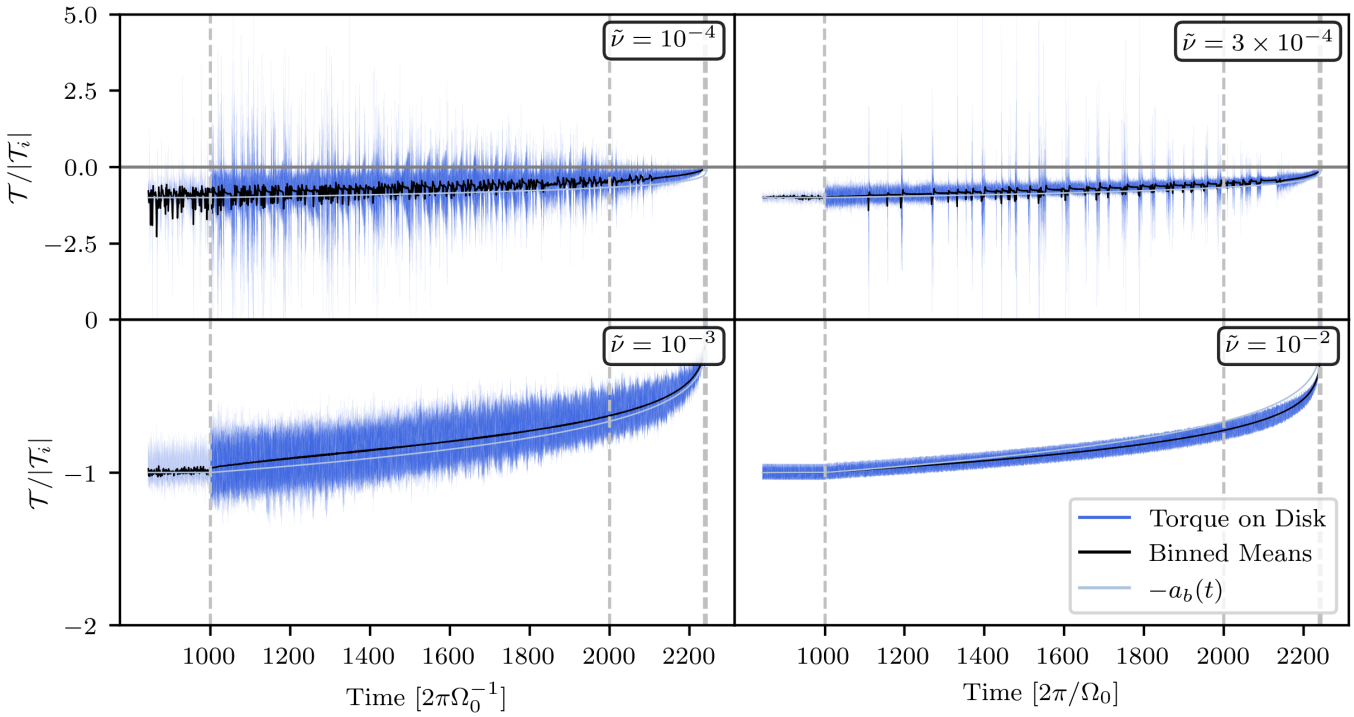

Figure 6. The torque exerted on the disk by the binary (blue) is normalized by the magnitude of the steady-state value determined during the burn-in phase $|\mathcal{T}_i|$. A negative torque means that the disk is losing angular momentum to the binary. The black line denotes the binned means of the torque, while the light blue line denotes (minus) the binary semimajor axis $-a_b(t)/a_0$. Similar to the accretion rates, less viscous disks (top) exhibit strong variability in their torque profiles, while larger viscosities (bottom) correspond to more regular profiles.

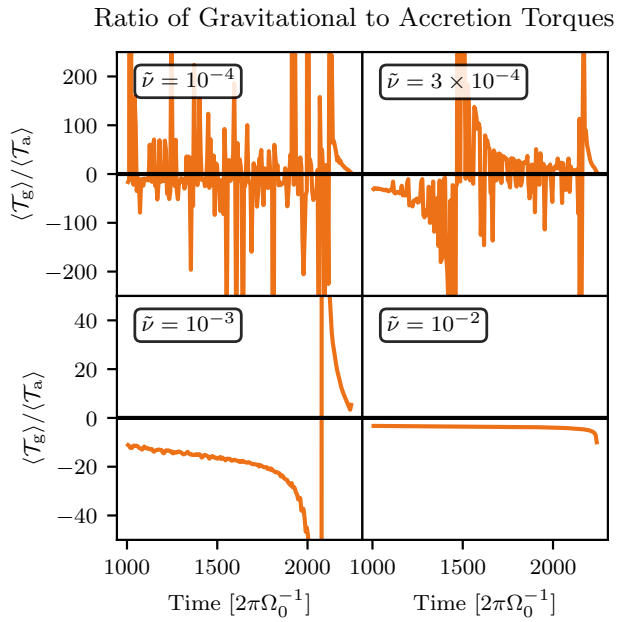

Figure 7. The ratio of averaged gravitational torques to averaged accretion torques taken over fixed time intervals of $\delta t = 12\pi\Omega_0^{-1}$. The dashed gray lines at $t = 1000$ $[2\pi\Omega_0^{-1}]$ denote the start of the orbital inspiral.

throughout the inspiral. This suggests that for highly viscous disks, the diminishing accretion rate is not due to the inadequate viscous transport of material, but rather the binary's own inefficiency at accreting gas because of the time-varying torque between the binary and the disk.

This weakening-torque effect as it manifests here is described by the Type A inspiral models of J. Zrake et al. (2025), where the disk is in-net delivering angular momentum to the binary. In this scenario, the inner regions of the disk are depleted relative to a disk that is experiencing no external torques (to accommodate the loss of angular momentum and centrifugal support). As the binary loses angular momentum to gravitational waves, the magnitude of the torque exerted by the binary decreases, and the disk will start to replenish its inner annuli. Mass conservation dictates that while the inner regions accumulate material (at a fixed supply rate), the accretion rate across the disk's inner edge must drop. This attenuates the mass flow to the binary, causing the accretion rate to continuously diminish as the strength of GW emission grows. For a retrograde configuration, this is consistent with disk-driven orbital decay because the disk delivers angular momentum to the binary, but the binary angular momentum is of opposite sign, so the orbit shrinks. Thus, when the binary evolves due to gravitational radiation, the system is of Type A and should present a power-law decay of the accretion rate. This is precisely what is observed, and when we directly compare to the J. Zrake et al. (2025) model, we find that the weakening-torque effect accurately describes our accretion rate decay during inspiral (dashed blue lines in Figure 5).

In Figure 6, the magnitude of the total torque exerted by the binary on the disk decreases as the system approaches merger. The declining binary semimajor axis reduces the lever arm, resulting in a weaker torque ($\mathcal{T} = a_b F_\theta$), as illustrated by the light blue lines in Figure 6. Correspondingly, the azimuthal force between the binary and the disk (F_θ) remains approximately constant throughout the inspiral. We note that for a circular binary, the power exerted on the disk is proportional to the torque, given by $\mathcal{P} = \Omega\mathcal{T}$. As the orbital frequency increases, the magnitude of the power grows, reaching its maximum at the point of merger.

Figure 7 illustrates the ratio of the gravitational torque ($\mathcal{T}_g = -\boldsymbol{a}_b \times \boldsymbol{F}_g$) to the accretion torque ($\mathcal{T}_a = -\boldsymbol{a}_b \times \boldsymbol{F}_a$) for various viscosities throughout the inspiral. The ratio $\langle \mathcal{T}_g \rangle / \langle \mathcal{T}_a \rangle$ typically falls below -1, indicating that accretion and gravitational torques often act in opposition to each other, with the gravitational torques typically being the dominant component. This opposing relationship is reflected in Figure 3, where the intrabinary bridge attaches to the rear of the massive body, funneling accreted material into the sink from the direction trailing the binary's motion. As this material carries momentum in the direction of motion of the binary, its accretion generates a positive torque, contrasting with the always-negative gravitational torque.

Notably, for $\tilde{\nu} = 10^{-3}$ (lower left panel of Figure 7), the ratio between the gravitational torques and accretion torques diverges at $t \approx 2050\,[2\pi/\Omega_0]$. This divergence can be attributed to a sign change in the accretion torque, driven by an instability in the intrabinary bridge. Specifically, the bridge transitions from rear-attaching to front-attaching, causing the accreted material to enter from the front, thus reversing the direction of the momentum flux and changing the torque from positive to negative.[11] At very low viscosities $\tilde{\nu} = 10^{-4}$ (upper left panel of Figure 7), these instabilities become very frequent, and the divergences associated with them produce irregularities in the time series data, without any salient features. At moderately low viscosities $\tilde{\nu} = 3 \times 10^{-4}$ (upper right panel of Figure 7), there is a combination of short and long timescale bridge instabilities, in which the bridge is, on average, shifting its position, while still experiencing shorter-term instabilities causing divergences in the torque ratio. The stability of the bridge is thus understood to be a viscosity-dependent phenomenon and discussed in further detail in Section 4.2.

3.4. The Decoupling Process

We next discuss the process of decoupling for both prograde and retrograde circumbinary disks. In Figure 8, we plot the cavity semimajor axis as a function of the binary semimajor axis on a logarithmic scale.

At early times, the cavity is capable of tracking the binary's inspiral. This is demonstrated by the power-law relationship, $a_c \propto a_b^p$ for $p \approx 1$. At late times, the cavity enters a plateau, conveying the disk's inability to follow the binary. Between these two regimes, there exists an intermediate state where the power-law "breaks," signifying the decoupling of the binary from the disk. The analytical model given by Equation (10) predicts that this break occurs between binary semimajor axes of $33r_G$ and $3r_G$ for the viscosities considered in our simulations and assuming $\xi = 0.5$ as observed for retrograde central cavities. We compare this analytical model (vertical, faded lines) with our numerical results in Figure 8. We note that our results for prograde decoupling are in good agreement with Figure 2 of A. J. Dittmann et al. (2023).

Both prograde and retrograde disks exhibit similar decoupling profiles, breaking at comparable semimajor axes in Figure 8. We thus expect any observational signatures of decoupling to occur at a time set by the viscosity, not the orbital configuration of the disk. Consequently, time-domain

[11] We note that the divergence in the torque ratio does not precisely align with the instability in the intrabinary bridge. While most accreted material is funneled through the bridge, some accreted gas is not. Therefore, zero accretion torque does not correspond to the exact moment of bridge instability.

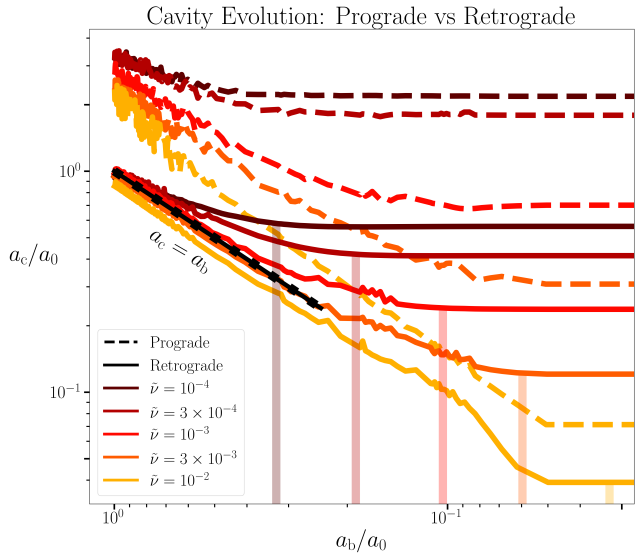

Figure 8. A logarithmic plot of the cavity semimajor axis a_c as a function of the binary semimajor axis a_b throughout the inspiral (early times to the left, later times to the right). The dashed and solid lines represent prograde and retrograde disk configurations, respectively, while the different colors represent different kinematic viscosities. The vertical faded lines denote the predicted decoupling semimajor axis from Equation (10) with $\xi = 0.5$, while the black overlay line traces the cavity evolution during the coupled-phase of binary-disk evolution.

measurements could infer the viscosity by measuring the time of decoupling (the time of decoupling is expected to coincide with a change in the EM signature, e.g., L. M. Krauth et al. 2023) without knowing the sense of rotation of the circumbinary disk a priori. Furthermore, the point of decoupling is likely to be within the LISA band (A. J. Dittmann et al. 2023, depending on the black hole masses and disk viscosity) enabling triggered measurements of the event through multimessenger astronomy. Finally, we note that the break in the power law is smooth rather than sharp, suggesting that decoupling is a gradual process and may be accompanied by long-term EM variability (see J. Zrake et al. 2025, for further discussion).

The main difference between the two circumbinary disk configurations in Figure 8 is the size of the cavity, which is invariably smaller for retrograde disks. A smaller cavity enables gas to reach deeper into the potential well of the binary, which may lead to the emission of high-frequency EM radiation from the circumbinary disk (enhanced UV, for example). We note, however, that the lack of minidisks may result in a reduction (or absence) of the highest frequencies of X-ray emission.

4. Discussion

4.1. The Stability of Retrograde Orbits

Retrograde disks display a small central cavity, suggesting an enhancement in the orbital stability for retrograde circumbinary test particles. In order to gain intuition for the size of the cavity, we review the restricted three-body problem (R3BP) for disk particles around an equal-mass binary.

In the R3BP, we consider a small test particle $m \ll M$ moving with velocity v in the binary's corotating frame of reference. We center our coordinate system on the barycenter from which the test particle is a radial distance r away. In this

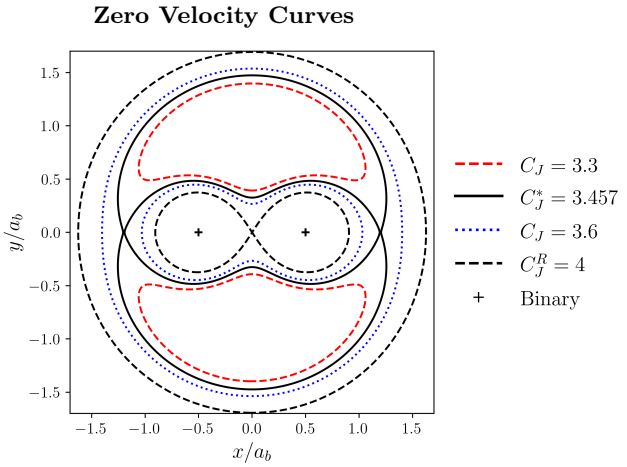

Figure 9. Zero-velocity curves for different values of the Jacobi constant C_J. The critical value C_J^* (solid black line) is the minimum value that separates the binary (black dots) from the outer regions of the disk. For $C_J < C_J^*$ (red dashed line), a particle can cross through L_2 or L_3 to travel between the inner and outer regions of the disk. The Roche-bound region (dashed black line) is described by an isocontour C_J^R and describes test particles that are bound to one of the binary components.

non-inertial frame, the particle evolves under an effective potential $U_{\rm eff}$,

$$U_{\rm eff} = \frac{m\Omega_{\rm b}^2 r^2}{2} + \frac{GM}{2r_1} + \frac{GM}{2r_2}, \tag{11}$$

where r_1, r_2 are the radial distances to the two binary components and $\Omega_{\rm b}$ is the binary's orbital frequency. While the total energy and momentum are globally conserved, the only locally conserved quantity (i.e., for each test particle individually) is the Jacobi constant C_J defined as,

$$C_J = 2U_{\rm eff} - v^2. \tag{12}$$

As a constant of motion, C_J is equal at all points along the particle's trajectory. In particular, when evaluated at $v = 0$, the Jacobi constant traces isocontours of the effective potential known as the "zero-velocity curves" (ZVCs). These ZVCs cannot be crossed, as doing so would require a negative squared velocity. Therefore, these curves delineate the edges of spatial domains accessible to the test particle and confine it to within the bounds of its ZVC. We illustrate four different examples of ZVCs (corresponding to different values of the Jacobi constant) in Figure 9. The critical value of the Jacobi constant C_J^* (D. J. D'Orazio et al. 2016) encloses the binary (black dots) and separates it from the outer regions of the disk. For subcritical Jacobi constants ($C_J < C_J^*$ red, dashed lines), test particles can cross from the inner to the outer disk through the Lagrange points L_2 or L_3. Meanwhile, for supercritical Jacobi constants ($C_J \geqslant C_J^*$, blue dotted lines), test particles cannot cross between the inner and outer disk. Therefore, particles with subcritical Jacobi constants can be expelled by the binary in the process of cavity formation, whereas particles with supercritical Jacobi constants cannot, thus limiting the extent of gap clearing. The isocontour C_J^R (black, dashed line) delineates the binary's Roche-bound region, within which particles with $C_J > C_J^R$ are bound to an individual component

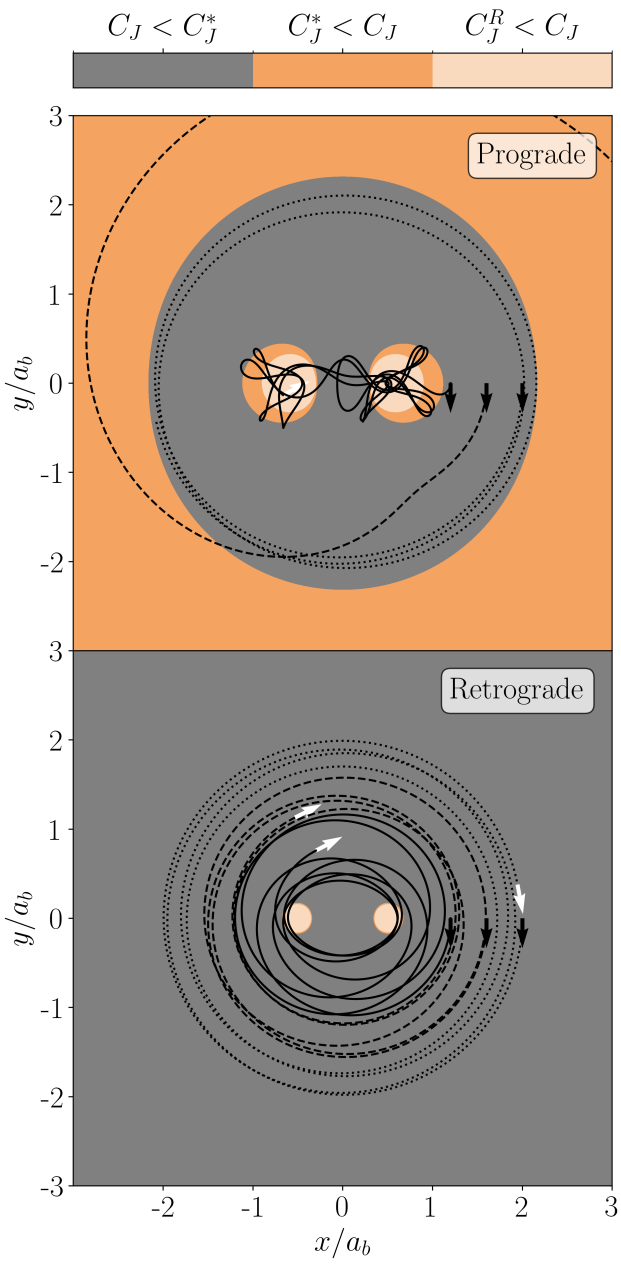

Figure 10. Subcritical (gray), supercritical (orange), and Roche-bound (beige) values of the Jacobi constant for prograde (top) and retrograde (bottom) Keplerian disks. The solid, dashed, and dotted lines are tracks of test particles in the corotating frame, initialized on circular Keplerian orbits at radii $r/a_0 = 1.2, 1.6, 2$. The black and white arrows denote the particle's initial and final positions, respectively.

of the binary. This Roche-bound region is an approximation of the maximum size attainable by the circumsingle minidisks.

We compute the values of the Jacobi constant for prograde ($-$) and retrograde ($+$) Keplerian disks by prescribing the velocity profile in the corotating frame $v_{\rm K,\pm}$,

$$v_{\rm K,\pm} = \Omega_{\rm b} r \pm \sqrt{\frac{GM}{r}}. \tag{13}$$

In Figure 10 we segregate Keplerian disks into the regions of subcritical (gray), supercritical (orange), and Roche-bound (beige) Jacobi constant values. This illustrates the disk regions that are more susceptible to being cleared by the prograde

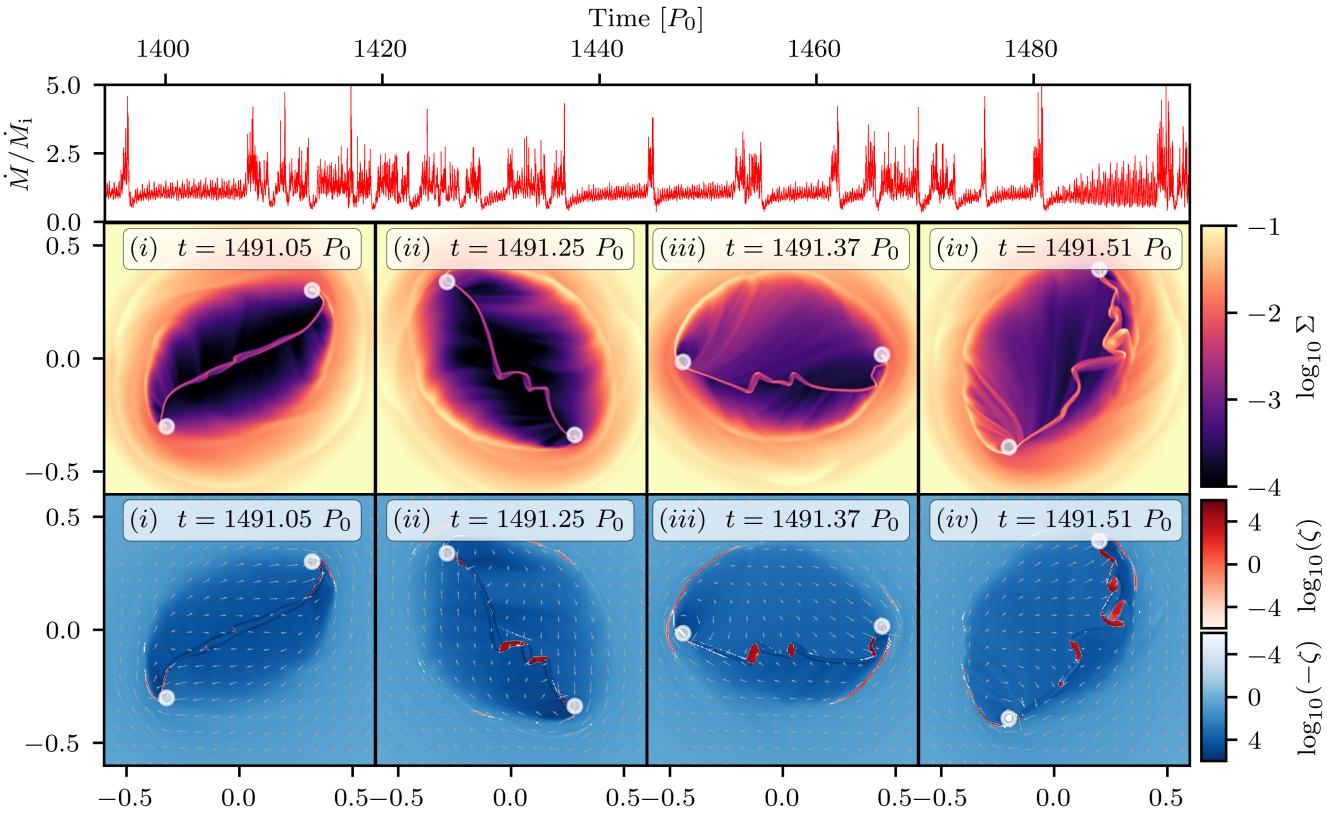

Figure 11. The normalized accretion rate (top), disk surface density (middle), and vortensity (bottom) during a phase of bridge instability (gray band) for $\tilde{\nu} = 10^{-4}$. The arrows illustrate the velocity profile of the disk, while the white circles represent the component sinks. The vortensity can be either aligned (red) or misaligned (blue) with the binary angular momentum vector. The white vectors illustrate the local gas velocity while the binary moves counterclockwise. The time in each panel is expressed in units of the initial orbital period $P_0 = 2\pi\Omega_0^{-1}$.

binary (gray) and those that are more resilient (orange, beige). While insightful into the dynamics, the Jacobi constant analysis does not provide a measure of orbital stability other than whether a particle can be expelled or not. To quantify the stability of orbits within the subcritical regions, we numerically integrate the orbits of three test particles in Figure 10 using an adaptive time step Runge–Kutta–Fehlberg method, a fourth-order integrator with fifth-order error estimation. We conserve the Jacobi constant to a fractional error of less than 10^{-4} for each particle over the course of the integration (∼three binary orbits).

Retrograde disks have a subcritical region (gray) extending outward from $r \approx 0.7a_b$ in Figure 10. Test particles within this region are stable (M. H. M. Morais & C. A. Giuppone 2012), almost down to the binary semimajor axis. In contrast, the subcritical region in prograde disks is truncated at radius $r \approx 2a_b$, wherein test particle orbits are unstable and can be ejected (see Figure 10 and Figure 5 of D. J. D'Orazio et al. 2016). In the outer supercritical region (orange), material is unable to access the inner regions of the disk and, therefore, unable to replenish the cavity created by ejected particles. We note that for a collisional medium (where the mass of the particles is nonnegligible), A. Mastrobuono-Battisti et al. (2025) found that prograde orbits form closer to the center than retrograde ones. Finally, we note that the radius of the Roche-bound regions (beige in Figure 10) is $r_{RL} \approx 0.15a_b$ for retrograde disks and $r_{RL} \approx 0.31a_b$ for prograde disks, in agreement with the discussion presented in Section 3.1.

4.2. Bridge Instabilities

Low-viscosity retrograde disks exhibit quasiperiodic flaring, corresponding to phases in which the accretion rate and torque sharply rise. Coincident with these flares are dynamical instabilities in the intrabinary bridge, where it dislodges and restabilizes a few orbits later. We illustrate an example of this instability in Figure 11.

The intrabinary bridge serves as an interface between two regions of the disk, where the direction of flow reverses. This reversal results in a steep velocity gradient, making the bridge prone to Kelvin–Helmholtz (KH)-like instabilities. We propose that the vortices generated by the KH mechanism act as a driving source for this instability. To capture the vortex structure along the intrabinary bridge, we illustrate the disk surface density and vortensity ($\zeta = \Sigma^{-1}(\nabla \times \boldsymbol{v})$) in Figure 11 over a series of times during the instability.

In column (i), the bridge is in a stable configuration with a steady accretion rate (gray band, top row of Figure 11). In column (ii), vortices emerge along the intrabinary bridge (bottom row), causing it to knot and twist as they propagate toward the sinks. By column (iii), these vortex-induced kinks have displaced the bridge from its natural equilibrium, allowing it to lopsidedly sway out of place. In column (iv), the sway of the bridge becomes more pronounced as it moves further from equilibrium, colliding with the cavity wall and disrupting the flow of gas in the circumbinary disk. In this column, the bridge instability is apparent, characterized by complicated gas dynamics and a dislodged intrabinary bridge.

Similarly, the instability is reflected in the accretion time series by a flare occurring at $t \approx 1491.5$ $[2\pi\Omega_0^{-1}]$. This behavior only manifests at low viscosities as vortex generation is suppressed for more viscous disks, and as a result, the bridge remains more stable. We note that C. Tiede & D. J. D'Orazio (2023) did not see this behavior due to a higher kinematic viscosity ($\tilde{\nu} = 10^{-3}$).

We find little to no sensitivity on the inner boundary sinks, with the instability persisting for (a) different sink prescriptions (both acceleration-free and torque-free, see A. J. Dittmann & G. Ryan 2021) and (b) lower sink rates (for $\gamma_{\rm sink} = 1$ and 50). Additionally, the instability persists for higher spatial resolution (increased to $n = 6000 \times 6000$ over the same domain). The instability even occurs during the gentle-sink period, meaning that when the sink is surrounded (and buffered) by the minidisk, the bridge can still become unstable, affirming that the sink has little role in sourcing the dynamics. In addition, the gentle-sink period is at a time before the inspiral has begun, ruling out any effects from asymmetries associated with the triangular Lagrange points L_4 and L_5 drifting from their fixed positions (J. D. Schnittman 2010). Therefore, it appears that the accretion flares and bridge instabilities are sourced by underlying physical processes rather than numerical artifacts and are unrelated to the inspiral.

Although the bridge instability is not sourced by the binary inspiral, it becomes more extreme at later times. During these late times, the intrabinary bridge can never stabilize (for low viscosities), as evidenced by flares in Figure 5 and visible in Figure 1. Without the typical cycle into and out of equilibrium, the accretion rate remains in a constant state of large variability.

4.3. Observational Appearance

Gravitational wave inspirals in prograde and retrograde disks share several similarities while also exhibiting significant variations. We briefly discuss the prospect of using EM observations to distinguish between the two disk configurations.

While decoupling occurs at nearly equal times between prograde and retrograde disks (for equal viscosities), the cavity plateau is noticeably lower for retrograde disks (see Figure 8). Therefore, signatures of retrograde disks may include:

1. Higher frequency EM emission from the circumbinary disk at the point of decoupling (and prior), likely resulting in increased optical and UV luminosities,
2. A shorter cavity closing timescale, or equivalently, a shorter "rebrightening" timescale after merger.

As a simple analytical estimate of the rebrightening timescale, we compute the cavity's viscous time $t_{\rm close} = a_{\rm c}^2/3\nu$ based on the semimajor axis it had in Figure 12 at decoupling.

The eccentric, lopsided nature of prograde cavities may enable some material to reach the merged remnant before τ_ν in Figure 12. Nonetheless, a full rebrightening will require the entire cavity to have closed, possibly taking an order of magnitude longer to occur for a prograde disk than a retrograde one, potentially providing a way to distinguish between both disk configurations. The ratio of rebrightening timescales is not monotonic with viscosity, peaking around $\nu = 3 \times 10^{-4} a_0^2 \Omega_0$ and declining for larger viscosities—suggesting that the size of prograde and retrograde cavities does not scale equally with viscosity. In addition, retrograde

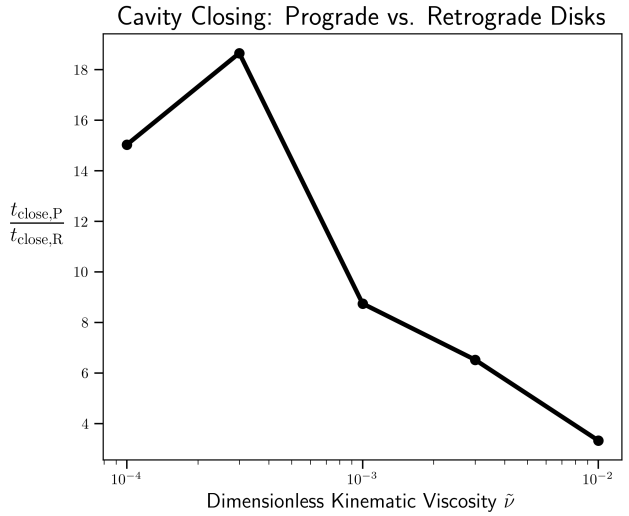

Figure 12. The ratio of prograde to retrograde cavity closing timescales (or disk rebrightening), following merger. These timescales are based on the cavity semimajor axes at decoupling (given in Figure 8).

merger remnants may have intrinsic spin oriented oppositely to the rotation of the refilling disk (e.g., M. Garg et al. 2024a), resulting in a larger ISCO than prograde mergers. The refueling ISCO is potentially observable via FeK-α line measurements (C. Fanton et al. 1997) if sufficiently bright, providing another way to distinguish between the two disk configurations.

The appearance of the intrabinary bridge may be a distinguishing feature of retrograde circumbinary disks. The shocked gas will likely produce the highest frequencies of EM radiation, which could be lensed by the binary and Doppler boosted by its dynamics (D. J. D'Orazio & Z. Haiman 2017; D. J. D'Orazio et al. 2024). In addition, the quasiperiodic flaring associated with bridge instabilities may be a general feature of low-viscosity retrograde disks and could appear as repeating nuclear transients characterized by X-ray flaring. It is important to note, however, that such flares may be less luminous than the bulk and background emission of the disk. A more careful analysis of the EM counterparts (T. Tanaka et al. 2010) accompanying SMBHB mergers in retrograde disks will require non-isothermal simulations, which is a topic left for future work.

5. Summary

We have performed 2D numerical hydrodynamic simulations of retrograde circumbinary disks, hosting an equal-mass binary undergoing gravitational wave inspiral. We have compared our results directly with prograde counterparts to better understand the differences between prograde and retrograde disk configurations. We found that:

1. Both prograde and retrograde disks decouple from the binary at comparable binary semimajor axes (for equal viscosities).
2. Retrograde central cavities are significantly smaller than prograde ones, explained by the presence of stable orbits close to the binary. This may lead to the circumbinary disk producing higher frequency emission at the point of decoupling. Additionally, this may cause the cavity to

close earlier postmerger, leading to a faster rebrightening of the disk.
3. Low-viscosity retrograde disks are prone to bridge instabilities, leading to quasiperiodic accretion flares. These may produce distinctive EM signatures of binaries in retrograde disks.
4. The lack of circumsingle minidisks may reduce the amount of high-frequency X-ray emission for retrograde disks, and may lead to different emission spectra than their prograde counterparts. In particular, because the disruption of prograde minidisks may signify a temporal signature of merging SMBHBs (e.g., an X-ray turnoff, L. M. Krauth et al. 2023), their absence for retrograde disks may alter such time-domain observables.

We highlight a number of simplifying assumptions made in this study. The prescribed binary dynamics in Equations (1) and (2) are an approximation to the full general relativistic equations of motion. In addition, the relativistic effects of gas dynamics have been neglected (V. Paschalidis et al. 2021; E. M. Gutiérrez et al. 2022; M. Ruiz et al. 2023; M. J. Avara et al. 2024), along with magnetic fields (S. C. Noble et al. 2012; R. Gold et al. 2014a, 2014b; E. R. Most & H.-Y. Wang 2024), radiation (L. del Valle & M. Volonteri 2018; D. J. Williamson et al. 2022; C.-H. Chan et al. 2025; V. Tiwari et al. 2025), jets and gravitational wave recoil kicks (L. M. Krauth et al. 2023; V. Manikantan et al. 2025; S. M. Ressler et al. 2025). Each of these phenomena will likely produce different observable consequences. The structure of the intrabinary bridge, the presence of mindisks, and overall disk morphology may differ for 3D simulations and larger Mach numbers than $\mathcal{M} = 10$, as adopted in this study (e.g., C. Tiede et al. 2020, 2025). Finally, we note that highly eccentric binaries embedded in massive retrograde disks have been observed to experience tilting instabilities (M. Garg et al. 2024a) in which the binary can reorient itself into a prograde configuration. Addressing these caveats is left for future work.

Acknowledgments

D.J.D., C.T., and D.O.N. acknowledge support from the Danish Independent Research Fund through Sapere Aude Starting grant No. 121587, led by D.J.D. We are grateful to the anonymous referee for the insightful comments and suggestions for improving the manuscript. This work was also supported in part by the LISA Preparatory Science Program (LPS) through NASA grant 80NSSC24K0440, by NASA Astrophysics Theory Program (ATP) grant 80NSSC22K0822, and by the European Union's Horizon research and innovation program under Marie Sklodowska-Curie grant agreement No. 101148364. This work made use of the following software packages: `Sailfish` (J. Zrake & A. MacFadyen 2024), `numpy` (C. R. Harris et al. 2020), `Python` (G. Van Rossum & F. L. Drake 2009), and `scipy` (P. Virtanen et al. 2020; R. Gommers et al. 2024). Software citation information aggregated using The Software Citation Station (T. Wagg & F. S. Broekgaarden 2024; T. Wagg et al. 2024). The Tycho supercomputer hosted at the SCIENCE HPC center at the University of Copenhagen was used in this work.

Appendix
Cavity Measurements

Following A. J. Dittmann et al. (2023), we define the central cavity to be the inner region of the disk with surface density less than $\Sigma_{\rm cav} = 0.2\Sigma_0$. To quantify the size of this region, we begin by constructing an isocontour of the surface density with value $\Sigma_{\rm cav}$. Along this contour, we sample 500 points (of the form $\boldsymbol{x}_i = x_i\hat{x} + y_i\hat{y}$ for $1 \leqslant i \leqslant 500$) which we seek to fit with an ellipse of semimajor axis $a_{\rm c}$, eccentricity $e_{\rm c}$ and argument of pericenter $\omega_{\rm c}$. Next, by defining the directed distance between points i and j as $\boldsymbol{d}_{\rm ij} \equiv \boldsymbol{x}_i - \boldsymbol{x}_j$, the cavity semimajor axis can thus be identified as,

$$a_{\rm c} = \frac{1}{2}\max(|\boldsymbol{d}_{\rm ij}|), \tag{A1}$$

corresponding to the maximum distance between any two points. We denote these two maximally distanced points $\boldsymbol{x}_-$ and $\boldsymbol{x}_+$, for which the argument of pericenter can be found as the relative angle between the two,

$$\omega_{\rm c} = \arctan\left[\frac{(\boldsymbol{x}_+ - \boldsymbol{x}_-)\cdot\hat{y}}{(\boldsymbol{x}_+ - \boldsymbol{x}_-)\cdot\hat{x}}\right]. \tag{A2}$$

To calculate the semiminor axis of the ellipse, we require the maximum distance of two points in a direction orthogonal to ω_c. We thus define the unit vector orthogonal to the argument of periapsis $\hat{n}$ as

$$\hat{n} = -\sin(\omega_{\rm cav})\hat{x} + \cos(\omega_{\rm cav})\hat{y}, \tag{A3}$$

for which the projected distance along this direction is given as $n_{ij} = \hat{n}\cdot\boldsymbol{d}_{ij}$. Hence, the semiminor axis of the ellipse $b_{\rm c}$ is given as

$$b_{\rm cav} = \frac{1}{2}\max(|n_{ij}|). \tag{A4}$$

Finally, using the semimajor and semiminor axes of the cavity, we calculate its eccentricity as

$$e_{\rm c} = \sqrt{1 - \frac{b_{\rm c}^2}{a_{\rm c}^2}}. \tag{A5}$$

ORCID iDs

David O'Neill https://orcid.org/0000-0002-1382-3802
Christopher Tiede https://orcid.org/0000-0002-3820-2404
Daniel J. D'Orazio https://orcid.org/0000-0002-1271-6247
Zoltán Haiman https://orcid.org/0000-0003-3633-5403
Andrew MacFadyen https://orcid.org/0000-0002-0106-9013

References

Afroz, S., & Mukherjee, S. 2024, JCAP, 2024, 42
Amaro-Seoane, P., Andrews, J., Arca Sedda, M., et al. 2023, LRR, 26, 2
Amaro-Seoane, P., Maureira-Fredes, C., Dotti, M., & Colpi, M. 2016, A&A, 591, A114
Armitage, P. J., & Natarajan, P. 2002, ApJL, 567, L9
Artymowicz, P., & Lubow, S. H. 1996, ApJ, 467, L77
Auclair, P., Bacon, D., Baker, T., et al. 2023, LRR, 26, 2
Avara, M. J., Krolik, J. H., Campanelli, M., et al. 2024, ApJ, 974, 242
Bankert, J., Krolik, J. H., & Shi, J. 2015, ApJ, 801, 114
Barnes, J. E., & Hernquist, L. E. 1991, ApJL, 370, L65
Begelman, M. C., Blandford, R. D., & Rees, M. J. 1980, Natur, 287, 307
Berczik, P., Merritt, D., Spurzem, R., & Bischof, H.-P. 2006, ApJL, 642, L21

Berentzen, I., Preto, M., Berczik, P., Merritt, D., & Spurzem, R. 2009, ApJ, 695, 455
Bogdanović, T., Miller, M. C., & Blecha, L. 2022, LRR, 25, 3
Bowen, D. B., Mewes, V., Campanelli, M., et al. 2018, ApJL, 853, L17
Casura, S., Ilić, D., Targaczewski, J., Rakić, N., & Liske, J. 2024, MNRAS, 534, 182
Chan, C.-H., Tiwari, V., Bogdanović, T., Jiang, Y.-F., & Davis, S. W. 2025, ApJ, 991, 71
Chandrasekhar, S. 1943, ApJ, 97, 255
Clyburn, M., & Zrake, J. 2025, MNRAS, 539, 1430
Cuadra, J., Armitage, P. J., Alexander, R. D., & Begelman, M. C. 2009, MNRAS, 393, 1423
del Valle, L., & Volonteri, M. 2018, MNRAS, 480, 439
DeLaurentiis, S., Haiman, Z., Westernacher-Schneider, J. R., et al. 2025, ApJ, 980, 55
DiMatteo, T., Ni, Y., Chen, N., Croft, R., & Pacucci, F. 2023, AAS/High Energy Astrophysics Division, 20, 103A.04
Dittmann, A. J., & Ryan, G. 2021, ApJ, 921, 71
Dittmann, A. J., Ryan, G., & Miller, M. C. 2023, ApJL, 949, L30
D'Orazio, D. J., & Charisi, M. 2023, arXiv:2310.16896
D'Orazio, D. J., & Duffell, P. C. 2021, ApJL, 914, L21
D'Orazio, D. J., Duffell, P. C., & Tiede, C. 2024, ApJ, 977, 244
D'Orazio, D. J., & Haiman, Z. 2017, MNRAS, 470, 1198
D'Orazio, D. J., Haiman, Z., Duffell, P., MacFadyen, A., & Farris, B. 2016, MNRAS, 459, 2379
D'Orazio, D. J., Haiman, Z., & MacFadyen, A. 2013, MNRAS, 436, 2997
Duffell, P. C., Dittmann, A. J., D'Orazio, D. J., et al. 2024, ApJ, 970, 156
Einstein, A. 1916, AnP, 354, 769
Fanton, C., Calvani, M., de Felice, F., & Cadez, A. 1997, PASJ, 49, 159
Farris, B. D., Duffell, P., MacFadyen, A. I., & Haiman, Z. 2015, MNRAS, 447, L80
Franchini, A., Bonetti, M., Lupi, A., & Sesana, A. 2024, A&A, 686, A288
Garg, M., Tiede, C., & D'Orazio, D. J. 2024a, MNRAS, 534, 3705
Garg, M., Tiwari, S., Derdzinski, A., et al. 2024b, MNRAS, 528, 4176
Gold, R., Paschalidis, V., Etienne, Z. B., Shapiro, S. L., & Pfeiffer, H. P. 2014a, PhRvD, 89, 064060
Gold, R., Paschalidis, V., Ruiz, M., et al. 2014b, PhRvD, 90, 104030
Gommers, R., Virtanen, P., Haberland, M., et al. 2024, scipy/scipy: SciPy v1.14.1, Zenodo, doi:10.5281/zenodo.13352243
Gong, Y., Luo, J., & Wang, B. 2021, NatAs, 5, 881
Gould, A., & Rix, H.-W. 2000, ApJL, 532, L29
Gültekin, K., & Miller, J. M. 2012, ApJ, 761, 90
Gutiérrez, E. M., Combi, L., Noble, S. C., et al. 2022, ApJ, 928, 137
Harris, C. R., Millman, K. J., van der Walt, S. J., et al. 2020, Natur, 585, 357
Hirsh, K., Price, D., Gonzalez, J.-F., Ubeira-Gabellini, M., & Ragusa, E. 2020, MNRAS, 498, 2936
Holz, D. E., & Hughes, S. A. 2005, ApJ, 629, 15
Kelley, L. Z., Blecha, L., & Hernquist, L. 2017, MNRAS, 464, 3131
Khan, F. M., Berentzen, I., Berczik, P., et al. 2012, ApJ, 756, 30
King, A. R., & Pringle, J. E. 2006, MNRAS, 373, L90
Kocsis, B., Haiman, Z., & Loeb, A. 2012, MNRAS, 427, 2680
Krauth, L. M., Davelaar, J., Haiman, Z., et al. 2023, MNRAS, 526, 5441
MacFadyen, A. I., & Milosavljević, M. 2008, ApJ, 672, 83
Mangiagli, A., Caprini, C., Volonteri, M., et al. 2022, PhRvD, 106, 103017
Manikantan, V., Paschalidis, V., & Bozzola, G. 2025, PhRvD, 112, 043004
Mastrobuono-Battisti, A., Seoane, P. A., i Alfonso, M. J. F., et al. 2025, A&A, 693, A22
Mayer, L. 2013, CQGra, 30, 244008
Miller, M. C., & Krolik, J. H. 2013, ApJ, 774, 43
Moody, M. S. L., Shi, J.-M., & Stone, J. M. 2019, ApJ, 875, 66
Morais, M. H. M., & Giuppone, C. A. 2012, MNRAS, 424, 52
Most, E. R., & Wang, H.-Y. 2025, PhRvD, 111, L081304
Muñoz, D. J., Miranda, R., & Lai, D. 2019, ApJ, 871, 84
Nixon, C. J. 2012, MNRAS, 423, 2597
Nixon, C. J., Cossins, P. J., King, A. R., & Pringle, J. E. 2011, MNRAS, 412, 1591
Nixon, C. J., King, A. R., & Pringle, J. E. 2011, MNRAS, 417, L66
Noble, S. C., Mundim, B. C., Nakano, H., et al. 2012, ApJ, 755, 51
Paschalidis, V., Bright, J., Ruiz, M., & Gold, R. 2021, ApJL, 910, L26
Peters, P. C. 1964, PhRv, 136, 1224
Ragusa, E., Alexander, R., Calcino, J., Hirsh, K., & Price, D. J. 2020, MNRAS, 499, 3362
Ressler, S. M., Combi, L., Ripperda, B., & Most, E. R. 2025, ApJL, 979, L24
Roedig, C., & Sesana, A. 2014, MNRAS, 439, 3476
Ruan, W.-H., Guo, Z.-K., Cai, R.-G., & Zhang, Y.-Z. 2020, IJMPA, 35, 2050075
Ruiz, M., Tsokaros, A., & Shapiro, S. L. 2023, PhRvD, 108, 124043
Schnittman, J. D. 2010, ApJ, 724, 39
Schnittman, J. D., & Krolik, J. H. 2008, ApJ, 684, 835
Schnittman, J. D., & Krolik, J. H. 2015, ApJ, 806, 88
Shakura, N. I., & Sunyaev, R. A. 1973, A&A, 24, 337
Siwek, M., Weinberger, R., & Hernquist, L. 2023, MNRAS, 522, 2707
Speri, L., Barsanti, S., Maselli, A., et al. 2024, arXiv:2406.07607
Springel, V., Yoshida, N., & White, S. D. M. 2001, NewA, 6, 79
Tamanini, N., Caprini, C., Barausse, E., et al. 2016, JCAP, 2016, 002
Tanaka, T., Haiman, Z., & Menou, K. 2010, AJ, 140, 642
Tanaka, T. L., & Haiman, Z. 2013, CQGra, 30, 224012
Tang, Y., Haiman, Z., & MacFadyen, A. 2018, MNRAS, 476, 2249
Tiede, C., & D'Orazio, D. J. 2023, MNRAS, 527, 6021
Tiede, C., Zrake, J., MacFadyen, A., & Haiman, Z. 2020, ApJ, 900, 43
Tiede, C., Zrake, J., MacFadyen, A., & Haiman, Z. 2025, ApJ, 984, 144
Tiwari, V., Chan, C.-H., Bogdanović, T., et al. 2025, ApJ, 986, 158
Van Rossum, G., & Drake, F. L. 2009, Python 3 Reference Manual (Scotts Valley, CA: CreateSpace)
Virtanen, P., Gommers, R., Oliphant, T. E., et al. 2020, NatMe, 17, 261
Wagg, T., Broekgaarden, F., & Gültekin, K. 2024, TomWagg/software-citation-station: v1.2, Zenodo, doi:10.5281/zenodo.13225824
Wagg, T., & Broekgaarden, F. S. 2024, arXiv:2406.04405
Wang, J.-M., Songsheng, Y.-Y., Li, Y.-R., & Du, P. 2022, MNRAS, 518, 3397
Westernacher-Schneider, J. R., Zrake, J., MacFadyen, A., & Haiman, Z. 2022, PhRvD, 106, 103010
Williamson, D. J., Bösch, L. H., & Hönig, S. F. 2022, MNRAS, 510, 5963
Zrake, J., Clyburn, M., & Feyan, S. 2025, MNRAS, 537, 3620
Zrake, J., & MacFadyen, A. 2024, Sailfish: GPU-accelerated grid-based astrophysics gas dynamics code, Astrophysics Source Code Library, ascl:2408.004
Zrake, J., Tiede, C., MacFadyen, A., & Haiman, Z. 2021, ApJL, 909, L13